EMBRY-RIDDLE
Aeronautical University™
SCHOLARLY COMMONS

Doctoral Dissertations and Master's Theses

Spring 5-2015

Supersonic Retro-Propulsion Computational Fluid Dynamics Analysis Applied to Future Mars Mission

Margarita Nataly Brandt
Embry-Riddle Aeronautical University

Follow this and additional works at: https://commons.erau.edu/edt

Part of the Mechanical Engineering Commons, and the Space Vehicles Commons

SUPERSONIC RETRO-PROPULSION COMPUTATIONAL FLUID DYNAMICS ANALYSIS APPLIED TO FUTURE MARS MISSION

By

Margarita Nataly Brandt

A Thesis Submitted to the College of Engineering Department of Mechanical Engineering in Partial Fulfillment of the Requirements for the Degree of Master of Science in Mechanical Engineering

Embry-Riddle Aeronautical University
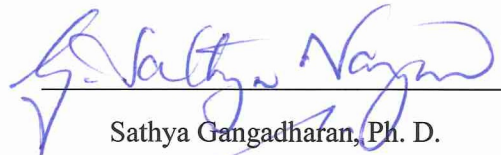
Daytona Beach, Florida

May 2015

SUPERSONIC RETRO-PROPULSION COMPUTATIONAL FLUID DYNAMICS ANALYSIS APPLIED TO FUTURE MARS MISSION
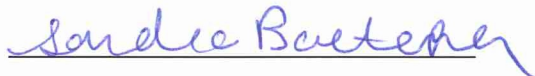
By

Margarita Nataly Brandt

This thesis was prepared under the direction of the candidate's Thesis Committee Chair Dr. Sathya Gangadharan, Professor, Daytona Beach Campus, and Thesis Committee Members Dr. Sandra Boetcher, Professor, Daytona Beach Campus and David Vaughan, Supervisor at Jet Propulsion Laboratory. It was submitted to the Department of Mechanical Engineering in partial fulfillment of the requirements of the degree of Master of Science in Mechanical Engineering.

Thesis Review Committee

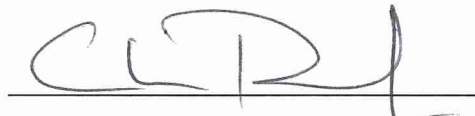Sathya Gangadharan, Ph. D.

Committee Chair

Sandra Boetcher, Ph. D.
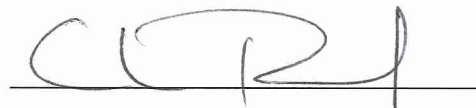
Committee Member

David Vaughan

Committee Member

Jean Michel Dhainaut, Ph.D.

Graduate Program Chair,

Mechanical Engineering

Charles F. Reinholtz, Ph. D.

Department Chair,

Mechanical Engineering

Maj Mirmirani, Ph. D.

Dean, College of Engineering

Robert Oxley, Ph. D.

Associate Vice President of Academics

ACKNOWLEDGMENTS

Abstract

Researcher: Margarita Nataly Brandt

Title: Supersonic Retro-Propulsion Computational Fluid Dynamics Analysis Applied to Future Mars Missions

Institution: Embry-Riddle Aeronautical University

Degree: Master of Science in Mechanical Engineering

Year: 2015

Supersonic Retro-Propulsion is one of the most promising emerging technologies being considered by NASA for use in future Mars missions. This new form of Entry Descent Landing has the potential to help increase the allowable payload mass currently constraining many science instruments and operations. Computational Fluid Dynamics was used to show the feasibility of supersonic retro-propulsion in Mars atmospheric conditions. The results presented show that SRP will be able to perform satisfactory using the same conditions that the Curiosity Rover was exposed to during its landing sequence. The plume expansion was analyzed for various cases, moving from free stream to supersonic conditions. Several computational methods were also examined to prove the model's accuracy. The mesh, physics models, and boundary conditions were ultimately selected based on the data obtained. The model was originally tested using a novel 1 dimensional software vetted and used by NASA. The bipropellant motor chosen has been flight proven and supported by data not presentable due to ITAR restrictions. The free stream and subsonic conditions analyses were primarily used to compare the supersonic results. The feasibility of supersonic retro-propulsion was proven in showing that even at the highest opposite flow Mach number analyzed, the effects on the main jet plume were negligible.

Table of Contents

List of Tables

List of Figures

CHAPTER 1
INTRODUCTION

1.1 <u>SRP Overview</u>

Future robotic and human missions to Mars will require larger payloads than past ones. Previous EDL techniques such as sphere-cone aeroshells and supersonic parachutes are currently being used but are not sufficient for future payload requirements. In order to land these larger masses, the propulsive capability currently used during subsonic descent needs to be extended to supersonic initiation velocities (Figure 1.1).

SRP descent requires rocket engine thrust to decelerate a lander from supersonic to subsonic conditions by increasing the total drag. There are three main advantages of SRP, the first being a decrease in design complexity since there are less aerodynamic decelerators and vehicle transitions used (Edquist,2007). This also eases the packing and deployment systems as the aerodynamic decelerators are small. The third advantage is the additional control as well as the ability to land larger payload masses.

SRP analysis began in the 1960s to 1970s, but was abandoned until recently because of the need for landing bigger payloads in Mars atmosphere. Most of the earlier work was focused on subscale wind-tunnel testing while recently it's been focused on CFD analysis and experimental testing. Early studies were done mainly on shock boundary and the effects of nozzle flow on boundary layer. The aerodynamic drag reduction in SRP was first observed by Jarvinen but was later validated through different experiments (Jarvinen, 1970).

Early SRP studies were not done using blunted-cone entry vehicles. However, they established the fundamentals of shock boundary layer theory. Early observations also demonstrated that increasing thrust coefficient moves the boundary layer transition closer to the nose of the vehicle. This initial work provided the basis for future wind tunnel testing.

There are still some technical challenges that need to be addressed in order for SRP to be a viable option for future Mars missions. The first main challenge is motor ignition in a supersonic counter flow. There is still no test data showing that this is possible, even with the small atmospheric pressure in Mars. Second, aerodynamics and

control are affected by the engine plume and external flow during SRP. Finally, convective and radiative heating due to the engine plume exhaust during EDL also need to be analyzed more in depth. These are specific challenges to SRP, however it also needs to overcome more general challenges such as landing strategies and flight demonstration.

Figure 1.1- SRP technology methods previously proposed

(Zang, T. A., *Entry, Descent and Landing Systems Analysis Study: Phase 1 Report*)

1.2 Background Theory

1.2.1- Model's parameters and assumptions

SRP adds a secondary flow to supersonic free stream in order to decrease the entry velocity of the payload. This creates a low velocity region with a low pressure around the jet and displaces the bow shock forwards (Figure 1.2). The following assumptions are made in order to simplify and analyze this problem:

- Flow is axially symmetrical
- Free stream consists of a perfect gas
- Jet is uniform and parallel to the exit plane
- No Reynolds number variations
- No heat transfer

The variables used are the motor/ free stream aerodynamic properties and the body/nozzle shape and size. Two other variables defined based on these inputs are the fineness $\lambda=a/b$ and the body Diameter $D=\frac{d_m}{d_j}$ (a, b= semi-axes of elliptical section parallel and normal to the free stream and $d_m= 2b$).
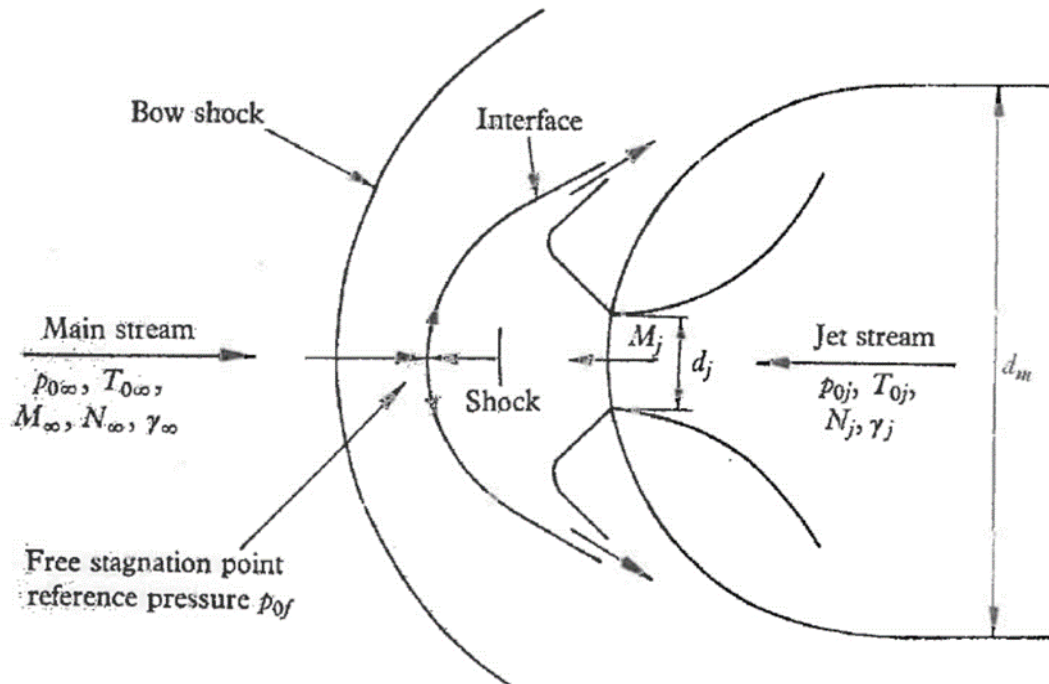
Figure 1.2- Flow parameters

(Cordell,CE. *Computations Fluid Dynamics and Analytical Modeling of Supersonic Retropropulsion Flowfield Structures Across a Wide Range of Potential Vehicle Configurations)*

The total pressure and temperature ratios are then calculated using: $P = \frac{P_{oj}}{P_{of}}$ and $T = \frac{T_{oj}}{T_{o\infty}}$. P_{of} is the total pressure after a normal and the reference pressure used for this analysis. The local surface Pressure depends mostly on P_{of} and surface inclination. This configuration gives a pressure distribution mostly independent of all free stream conditions (only depends slightly on M_∞). Therefore, as long as P_{of} remains constant, changes on free stream will only have a small effect on the pressure field because of the development of a mixing layer on the interface. The principal parameters taken into account are: D, λ, P, M_j and γ_j (N, γ_∞ and T are not used since one of the assumptions is no heat transfer).

1.2.2- Flow Description

The flow from the Solid R leaving from A, moves until it interferes with the mainstream at point B. The fluid is then deflected out and back over region C (the low velocity and pressure region) to a reattachment ring at E. This creates a shear layer were the fluid is entrained from Region C and returned to the reattachment ring. At point E, the Jet layer follows the model's surface and flows downstream. The pressure rise caused from the reattachment causes a turning shock at point G in the jet layer and free stream outside the interface.

Assuming a steady flow, the free stream and jet flow come to rest at the free stagnation point F. (where the Pitot Pressure=Pressure P_{of}). P_{oj} can't be less than P_{of} or there would be no outflow. When P>1, the bow shock moves forward and the body's pressure drops. Based on the Newtonian theory, P can be predicted by:

$$\frac{p}{p_{of}} = cos^2\theta + \frac{p_\infty}{p_{of}} sin^2\theta$$

At the low velocity region, θ increases, so P decreases to its minimum value P_d (dead-air pressure). It then increases to a maximum P_m at θ_m close to the reattachment point. At larger θ, Pr_{ST} is close to the value with no jet flow.
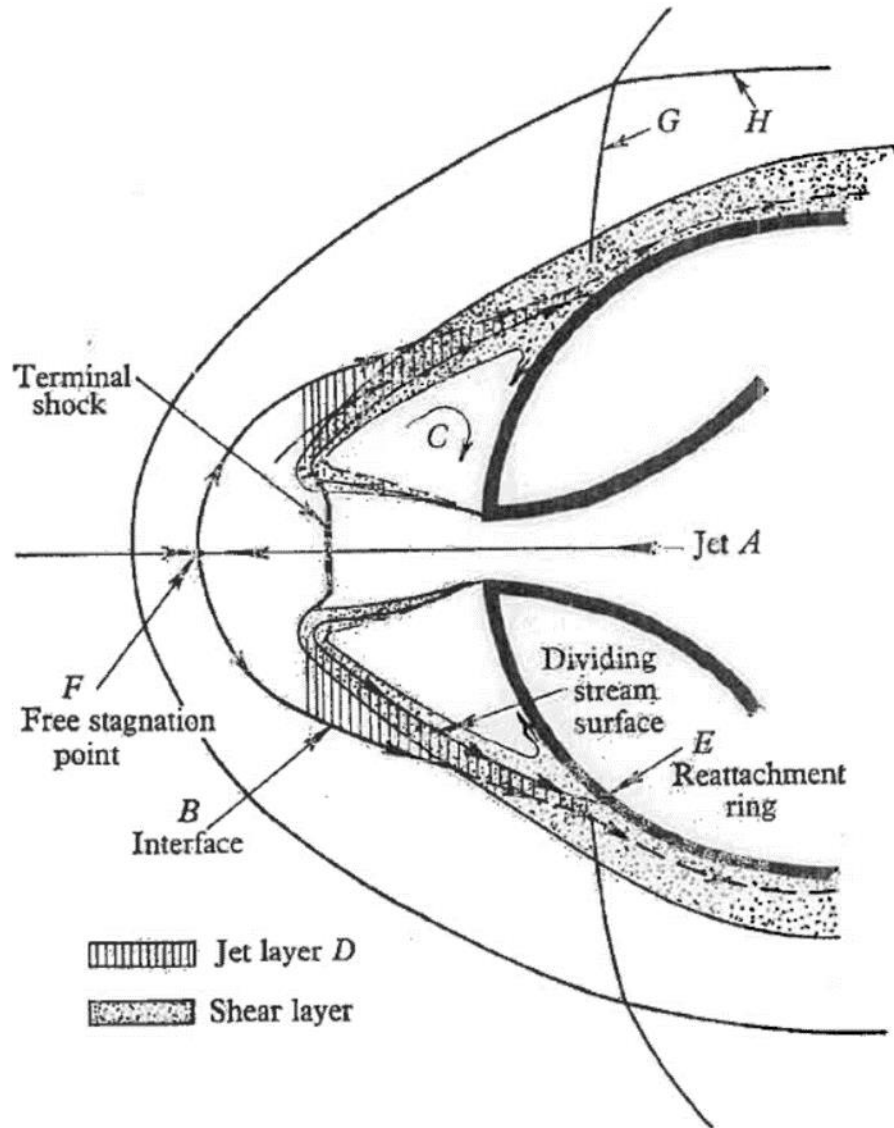
Figure 1.3- SRP flow interactions

(Cordell,CE. *Computations Fluid Dynamics and Analytical Modeling of Supersonic Retropropulsion Flowfield Structures Across a Wide Range of Potential Vehicle Configurations)*

1.2.3- Interface Momentum balance

The following assumptions are made for this analysis:

- Interface is a spherically blunted cone were the cone semi-apex angle = α and the Diameter=d_f.

- Φ= Local inclination of the surface to the free stream

- P_∞ = free stream static Pressure
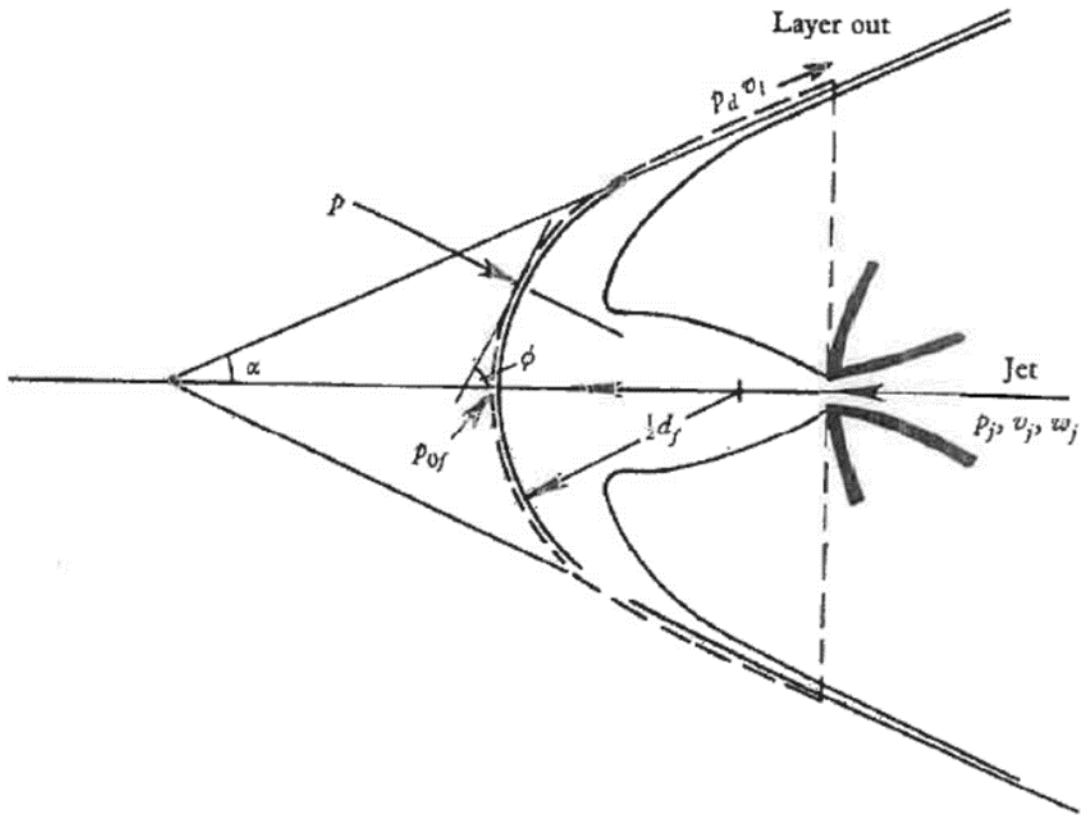
Figure 1.4- Control surface for force/momentum balance

(Charczenko, N., and Hennesey, K. W. "*Investigation of a Retrorocket Exhausting from the Nose of a Blunt Body into a Supersonic Freestream*")

The low velocity region (area between solid lines) pressure (P_d) is obtained using the modified Newtonian theory and provides this equation:

$$\frac{p_d}{p_{of}} = sin^2\alpha + \frac{p_\infty}{p_{of}}cos^2\alpha$$

P_d is constant through this region, except in the secondary flow's exit location where it is P_j. The following momentum-balance equation is obtained by integrating the interface region's pressure. The secondary flow's momentum is assumed to be such that the mass flow is expanded uniformly and isentropically from P_{of} to P_j.

$$\frac{1}{8}\pi d_f{}^2 cos^4\alpha\left(P_{of} - P_\infty\right) - \frac{1}{4}\pi d_j{}^2\left(P_j - P_d\right) = w_j v_j + w_l v_l cos\propto$$

*w_j and v_j: jet mass flow and exit plane velocity

*w_l and v_l: Jet layer mass flow and velocity leaving the control surface

*Jet flow force ➔ $F_j = \frac{1}{4}\pi d_j^2 (P_j) + w_j v_j$

Three other important functions used are:

- Flow force ➔ $G = \left(\frac{pA + wv}{w\sqrt{C_p T_o}}\right)$

- Mass flow ➔ $W = \frac{w\sqrt{C_p T_o}}{A p_o}$

- Velocity ➔ $V = \frac{v}{\sqrt{C_p T_o}}$

The jet flow equation can then be defined as:

$$F_j = \frac{G_j W_j}{\frac{1}{4}\pi d_j^2 p_{oj}}$$

After simplifications, the momentum equation turns into:

$$D_f^2 = P G_j W_j \left[1 + \frac{V_l}{G_j}\cos\alpha\right] Z^{-1} - \frac{p_d}{p_{of}} Z^{-1}$$

Where: $D_f = \frac{d_f}{d_i}$, $Z = \frac{1}{2}\cos^4\alpha\left(1 - \frac{p_\infty}{p_{of}}\right)$.

When P>5 (like in supersonic retro propulsion case), the second term can be neglected.

Also, $D = \frac{d_f}{d_m} = \left(\frac{d_f}{d_j}\right)\left(\frac{d_j}{d_m}\right)$. Therefore, when P is large, the momentum equation is:

$$\left(\frac{d_f}{d_m}\right)^2 = \left(\frac{PGW}{D}\right)^2 \left[1 + \frac{V_l}{G_j}\cos\alpha\right] Z^{-1}$$

The Jet flow coefficient is then used to simplify this equation, since:

$$C_F = \frac{F_j}{\frac{1}{4}\pi d_m^2 p_{of}} = \left(\frac{PGW}{D}\right)^2$$

The final Momentum equation is then:

$$\left(\frac{d_f}{d_m}\right)^2 = C_F \left[1 + \frac{V_l}{G_j}\cos\alpha\right] Z^{-1}$$

1.3 Computational Fluid Dynamics (CFD)

Computational Fluid Dynamics uses numerical methods to solve and analyze fluid flows problems. Different programs have been developed for this purpose, but they all work on the same basis: solving the Navier-Stoke equations (Figure 1.5). These equations

describe how the velocity, temperature and density of a moving fluid are related. These equations are very complex, but in theory, could be solved for any flow using calculus. Since they are too difficult to solve analytically, different techniques are used by computer programs to achieve a reasonable solution. Some solvers are pressure based while others are density based. Pressure based solvers were originally developed for low-speed incompressible flows. However, they have recently been reformulated to operate over a wider range of flow conditions. This approach extracts the pressure field by solving a pressure correction equation which is derived from the continuity and momentum equations.

Navier–Stokes Equations
3 – dimensional – unsteady
Glenn Research Center

Coordinates: (x, y, z)
Velocity Components: (u, v, w)

Time: t Pressure: p
Density: ρ Stress: τ
Total Energy: E_t

Heat Flux: q
Reynolds Number: Re
Prandtl Number: Pr

Continuity:
$$\frac{\partial \rho}{\partial t} + \frac{\partial(\rho u)}{\partial x} + \frac{\partial(\rho v)}{\partial y} + \frac{\partial(\rho w)}{\partial z} = 0$$

X – Momentum:
$$\frac{\partial(\rho u)}{\partial t} + \frac{\partial(\rho u^2)}{\partial x} + \frac{\partial(\rho u v)}{\partial y} + \frac{\partial(\rho u w)}{\partial z} = -\frac{\partial p}{\partial x} + \frac{1}{Re_r}\left[\frac{\partial \tau_{xx}}{\partial x} + \frac{\partial \tau_{xy}}{\partial y} + \frac{\partial \tau_{xz}}{\partial z}\right]$$

Y – Momentum:
$$\frac{\partial(\rho v)}{\partial t} + \frac{\partial(\rho u v)}{\partial x} + \frac{\partial(\rho v^2)}{\partial y} + \frac{\partial(\rho v w)}{\partial z} = -\frac{\partial p}{\partial y} + \frac{1}{Re_r}\left[\frac{\partial \tau_{xy}}{\partial x} + \frac{\partial \tau_{yy}}{\partial y} + \frac{\partial \tau_{yz}}{\partial z}\right]$$

Z – Momentum
Energy:
$$\frac{\partial(\rho w)}{\partial t} + \frac{\partial(\rho u w)}{\partial x} + \frac{\partial(\rho v w)}{\partial y} + \frac{\partial(\rho w^2)}{\partial z} = -\frac{\partial p}{\partial z} + \frac{1}{Re_r}\left[\frac{\partial \tau_{xz}}{\partial x} + \frac{\partial \tau_{yz}}{\partial y} + \frac{\partial \tau_{zz}}{\partial z}\right]$$

$$\frac{\partial(E_T)}{\partial t} + \frac{\partial(u E_T)}{\partial x} + \frac{\partial(v E_T)}{\partial y} + \frac{\partial(w E_T)}{\partial z} = -\frac{\partial(up)}{\partial x} - \frac{\partial(vp)}{\partial y} - \frac{\partial(wp)}{\partial z} - \frac{1}{Re_r Pr_r}\left[\frac{\partial q_x}{\partial x} + \frac{\partial q_y}{\partial y} + \frac{\partial q_z}{\partial z}\right]$$
$$+ \frac{1}{Re_r}\left[\frac{\partial}{\partial x}(u\tau_{xx} + v\tau_{xy} + w\tau_{xz}) + \frac{\partial}{\partial y}(u\tau_{xy} + v\tau_{yy} + w\tau_{yz}) + \frac{\partial}{\partial z}(u\tau_{xz} + v\tau_{yz} + w\tau_{zz})\right]$$

Figure 1.5- Navier-Stokes Equations

The CFD process consists of three main steps. The first step, pre-processing, describes the geometry and fluid domain. The fluid domain is then divided into smaller segments in the mesh generation. The physics of the model, fluid components, properties and boundary conditions are also set in this first step. The second step is the solver. The

solver uses the physics information input in the previous step and solves the Navier-Stokes equations through iterations. The final step of the process is post-processing. During post-processing, the results are analyzed using plots, contour maps, streamlines and scalar and vector plots (STARCCM + Manual).

There are different CFD programs available to the public. Some of the most known are: ANSYS, FLUENT, STARCCM, CFD++ and Fun3D. This project uses StarCCM, which is a pressure based solver owned by CD-Adapco. It is widely used throughout the Aerospace industry because of its capabilities. This program solves the Navier-Stoke equations and the Shear Stress Transport (SST) equations for all iterations once all physics models and inputs are entered.

<center>**CHAPTER 2**</center>

<center>**PROJECT SET UP**</center>

2.1 Project description

       This work presents a conceptual SRP model consisting of a theoretical bipropellant jet plume flow meeting an opposing supersonic flow at Mars atmospheric conditions. The single engine design results presented demonstrate the feasibility of this technology for the range of free stream Mach number cases studied. Subsonic and Sonic cases were first analyzed to later be compared with Supersonic results. The Maximum free stream Mach number studied was 3. Even though higher Mach numbers are out of the scope of this project, they are still feasible based on the final results obtained. The motor used for all calculations was chosen based on previous data and testing. A similar design has already been used in space flight missions in the past.

2.2 Objectives

       The main objective of this study is to analyze the effect of an opposing Supersonic flow to a jet plume flow. The cases examined (Table 2.1) demonstrate the viability of utilizing SRP in future Mars landings through Pressure, Mach and Temperature Plots. The CFD analysis is initially validated using a prior TDK analysis, different Mesh sizes and turbulence models. The feasibility of technology is measured by the effect the opposing flow has on the main jet plume expansion compared to subsonic and free stream cases.

<center>**Table 2.1- Opposing flow Mach numbers analyzed**</center>

	Opposite free stream flow Mach Number
Free expansion	0
Subsonic	0.5
	0.9
Sonic	1

Supersonic	1.5
	2
	2.5
	3

2.3 Motor Specifications

The motor chosen for this analysis was a theoretical Bipropellant (MMH/NTO) motor with an $A_e/A_t = 100$ and 100lbf thrust. The throat conditions were used as inputs for the simulation (Table 2.2). At the throat, the total Pressure was 86.6 psi and the total Temperature 2017 K. In order to reduce the calculation time, only the 3 main exhaust components were taken into account for this simulation: CO, H_2O, N_2. The main reason to only take into considerations only the three main components was calculation time and computer power. The results obtained are still valid since all other components constitute less than 1% of the mixture (Table 2.3).

Table 2.2- MMH motor properties

	Chamber	Throat
$\dfrac{P_C}{P}$	1	1.76
P	150	86.6
T	3162 K	2017 K
C_p (gas)	0.49	0.49
γ (gas)	1.2284	1.2334
Mach Number	0	1

Table 2.3- MMH motor components/ mol and mass fractions

	Mole fractions	Mass fractions
CO	1.06E-01	1.36E-01
CO_2	5.22E-02	1.05E-01
H	2.54E-02	1.17E-03

HO_2	2.70E-05	4.10E-05
H_2	9.32E-02	8.61E-03
H_2O	3.49E-01	2.88E-01
H_2O_2	2.00E-06	3.00E-06
N	7.00E-06	5.00E-06
NH_3	1.00E-06	1.00E-06
NO	7.92E-03	1.09E-02
N_2	3.15E-01	4.04E-01
O	5.98E-03	4.38E-03
OH	3.70E-02	2.88E-02
O_2	8.89E-03	1.30E-02

The MMH theoretical motor's nozzle geometry was used for the model design. Because of ITAR restrictions, the entire nozzle profile cannot be shown in this report. However, the main design dimensions (Table 2.4) can provide an approximate picture of the nozzle size.

Table 2.4- MMH motor nozzle dimensions

$Throat\ radius$	0.0289 ft
$\dfrac{Throat\ Wall\ radius}{Throat\ Radius}$	2.63E-03
$\theta\ (deg)$	30º
$Nozzle\ expansion\ ratio$	100

2.4 Preliminary Design

2.4.1 CAD and CFD Model

The CAD model used in the CFD analysis was designed in NX. The nozzle was modeled using the dimensions provided by the MMH Nozzle geometry coordinates profile (ITAR Restricted). The dimensions were converted to inches for the ease of the design (Table 2.4 and Figure 2.1).

Table 2.5- MMH nozzle dimensions-inches

Throat radius	0.3468 in
Throat Area	0.3778 in^2
Nozzle exit radius	3.468 in
Nozzle exit Area	37.78 in^2
θ (deg)	30º
Nozzle expansion ratio	100
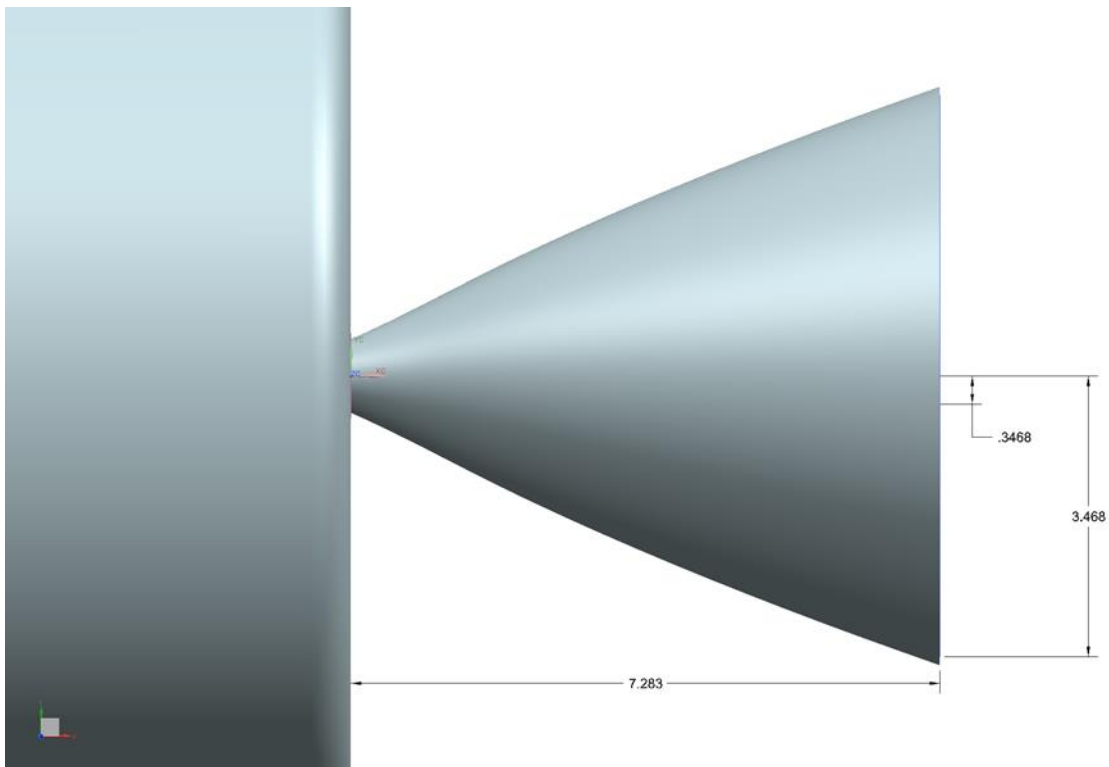
Figure 2.1- MMH nozzle CAD design

In order to use the final MMH design for the CFD analysis, an outside volume was created to represent the fluid flow. This outside volume with was designed taking into account the fluid's need to reach stability. The height and width dimensions (430 in x 600 in) were chosen taking into consideration the length needed for a complete plume expansion (Figures 2.2 and 2.3). For calculation time purposes, the CFD model only took into account 30º of the model. Reducing the total volume used for the calculations

decreases the number of cells, making it easier and faster for the solver to converge. This won't affect the final results because of the symmetric nature of the design.
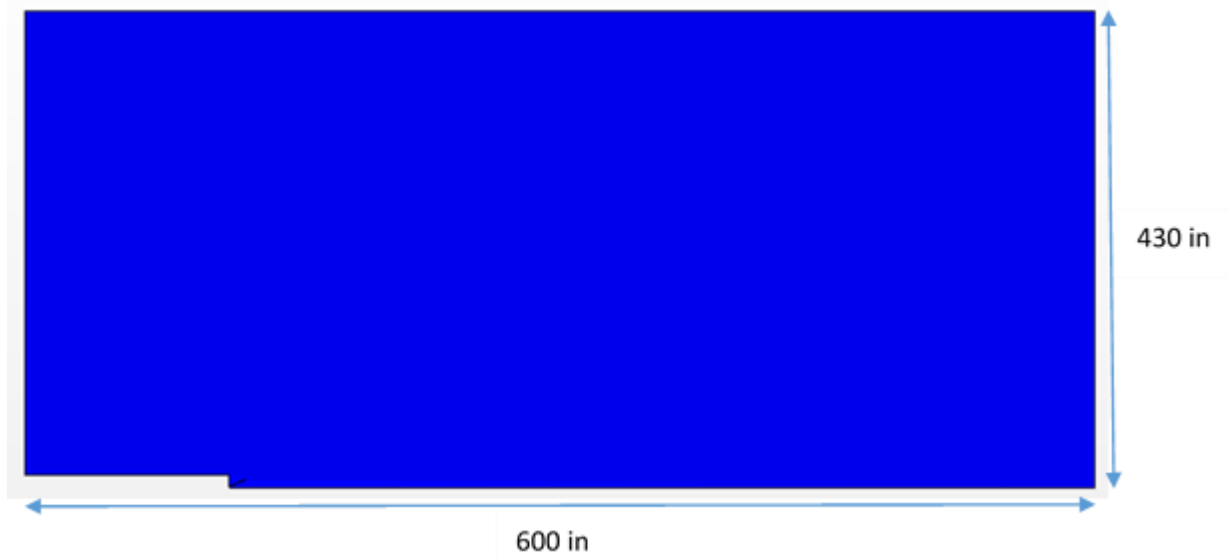
Figure 2.2- CFD Complete CAD Model
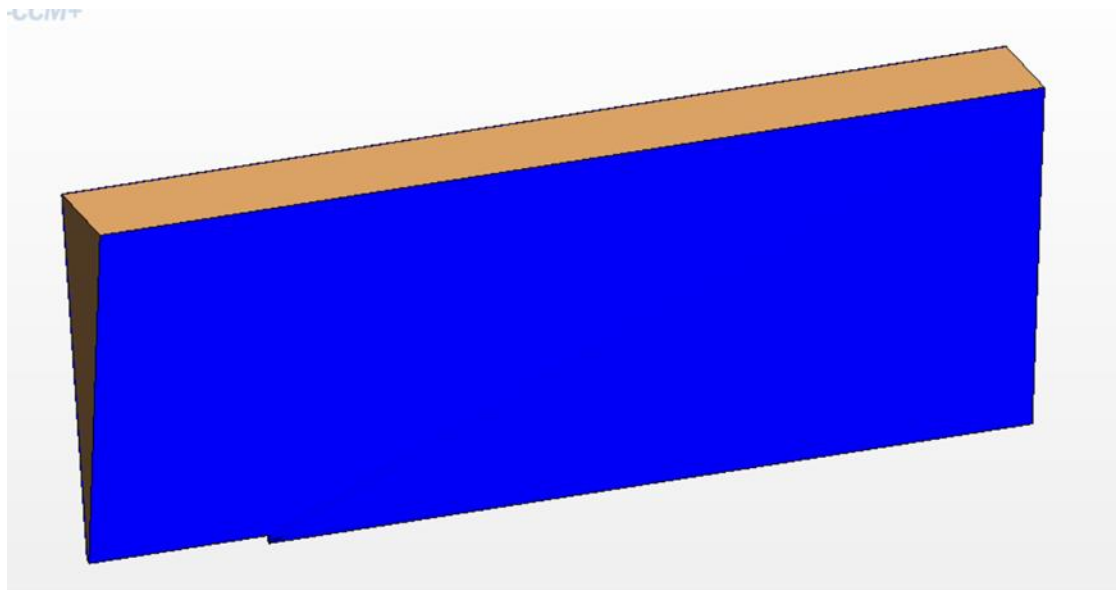
Figure 2.3- CFD volume used (30 degrees of model)

2.5 Theoretical Analysis results (TDK)

The theoretical 1-D analysis along the centerline of the nozzle provided results at different locations of the burn (Table 2.6 and Figure 2.4). The values of comparison are: Mach, Velocity, Temperature and Pressure. These results are later used to validate the CFD model initial results before applying the opposing supersonic velocity. The TDK analysis calculated the flow properties assuming it expands in a vacuum. This assumption is the main reason why the results obtained from this section don't coincide with the ones obtained from the initial CFD analysis. For the CFD calculations, an outside pressure needs to be present or in the contrary the solver equations diverge resulting in a floating point error.

Table 2.6- Theoretical Analysis Results

	Chamber	Throat	Exit A	Exit B	Exit C
$\dfrac{A_e}{A_t}$		1	15.03	50.00	100.00
$x(ft)$		0	0.17	0.38	0.60
$\dfrac{P_c}{P}$	1	1.79	1.00	853.41	2221.95
$P(psia)$	150	83.74	149.90	0.18	0.07
$T(Farenheit)$	5267.30	4675.30	5266.30	941.30	646.30
$\rho\left(\dfrac{lb}{ft^3}\right)$	5.33E-02	3.32E-02	5.32E-02	2.55E-04	1.24E-04
$\gamma(solid)$	1.23	1.23	1.23	1.32	1.34
$Velocity\left(\dfrac{ft}{s}\right)$	4003.70	3796.50	4003.30	2052.00	1835.40
$Mach\ number$	0	1	0.04	4.81	5.52
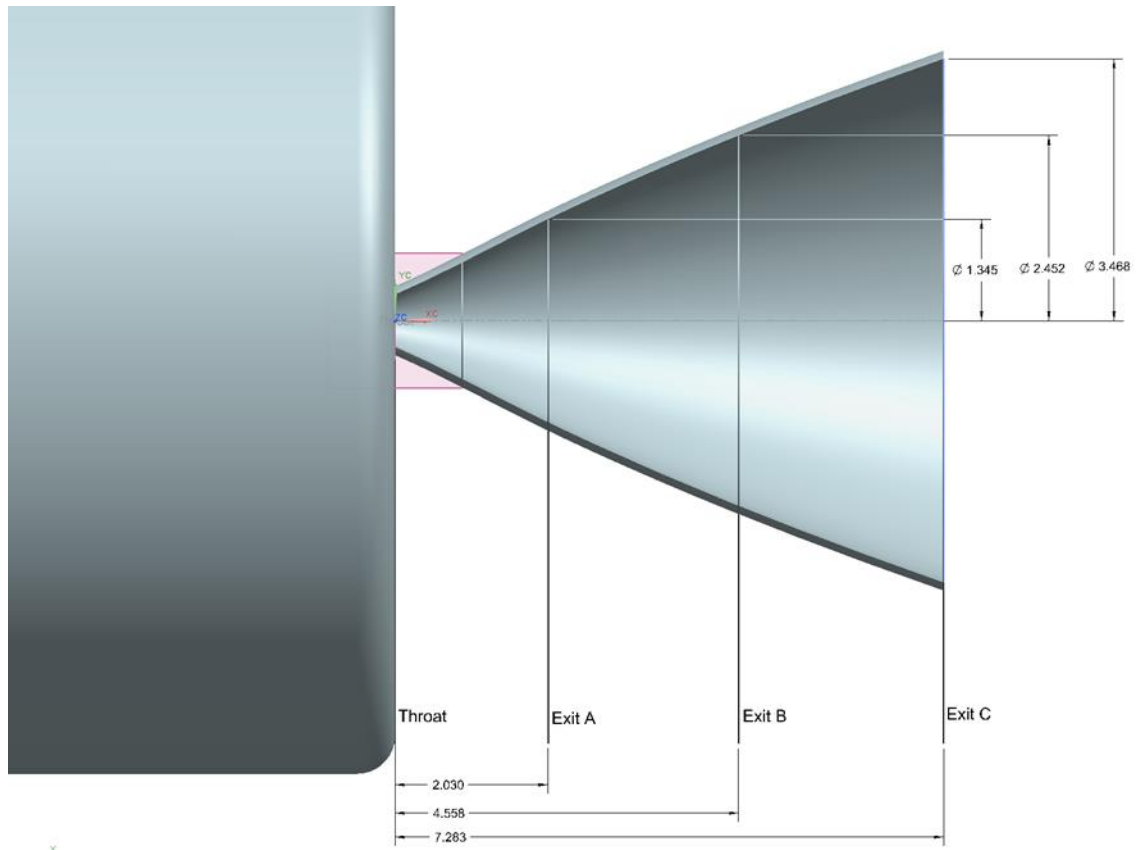
Figure 2.4- 1D exit properties

CHAPTER 3
CFD ANALYSIS

3.1 CFD Analysis Set Up

3.1.1 CFD general inputs

The Computational Fluid Dynamics (CFD) model was set up as a: 3 dimensional, turbulent, ideal gas coupled flow physics model. A complete list of the Physics Model is shown in Table 3.1. The results were validated using different mesh sizes and turbulence options for the free expansion case. In addition, these results were also compared to the free expansion results obtained from the TDK software. The cases with variable opposite flow Mach numbers (Table 1.1) were executed only for one mesh size and K-Omega turbulence in order to reduce the calculation time since each case required several hours to run. Each case was analyzed using 1st and 2nd degree coupled flow models, but only the 1st degree results are later shown. The 1st degree cases were mostly used as a way to decrease the calculation time by making the first iterations run faster.

Table 3.1- CFD Physics Model Properties

Physics Model Properties
All y + Wall treatment
Cell Quality Remediation
Coupled Energy
Coupled Flow
Coupled Species
Gradients
Gravity
Ideal Gas
K-Omega Turbulence- 1st order
Multi-Component Gas
Non-reacting
Reynolds-Averaged Navier Stokes

Steady
Three Dimensional
Turbulent

The jet flow properties (Table 2.1) and opposite free stream flow (Table 3.2) were used as inputs in the CFD model. The opposite flow used Mars atmospheric conditions at an altitude of 8 km. At this altitude, the Pr_o was approximately 0.04 psi and the T_o 260 K. Only the 3 main gas components: CO_2, Ar, N_2 were input into the model. However, these 3 compose more that 99.5% of the atmosphere. The flow's Mach number (Table 1.1) varied for each case.

Table 3.2- Mars free stream flow properties

Mars free stream Properties	
Pressure	0.04 psi
Gas components	CO2(0.96), Ar(0.02), N2(0.02)
Static Temperature	260 K
Mach number	variable

3.1.2 Mesh

3.1.2-a Initial mesh

A coarse mesh was used at the start of the analysis in order to make the simulation run faster (Table 3.3). Larger mesh elements reduce the calculation time, but the results obtained are also not very accurate. This mesh was basically just used as a start point to ensure the simulation would run properly with the final more detailed base mesh.

Table 3.3- Coarse Mesh properties

Coarse Mesh (Mesh 1)		
1	Number of Cells	304658
2	Number of faces	1944759
3	Number of Vertices	1672996

3.1.2-b Re-defined mesh

The redefined mesh was divided into different sections. The outside region had a mesh size of 60 mm, the plume 11 mm and the nozzle 3 mm (Figure 3.1). A comparison between both meshes shows that the detailed mesh has approximately 7 times more cells than the coarse mesh. This increases the calculation time, but also the accuracy of the results. The whole model is not composed of small cells since main areas of interest are the plume expansion and the nozzle region. These are the regions were calculation problems could be present once the supersonic opposite flow is introduced.
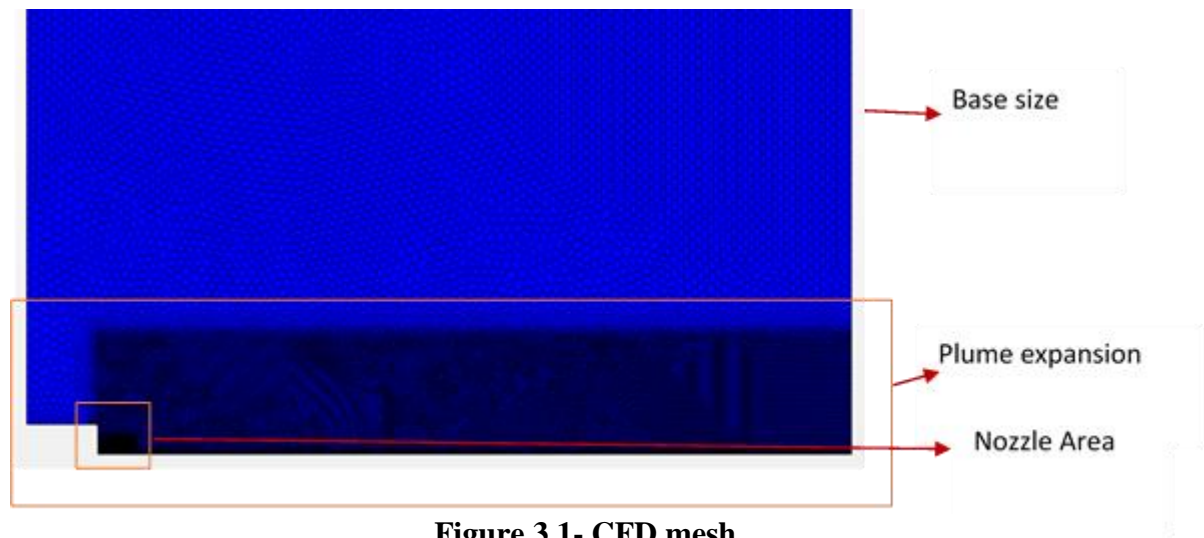

Figure 3.1- CFD mesh

Table 3.4- Comparison between meshes

	Mesh 1	Mesh 2
Total number of cells	304658	2388370
Base size	60 mm	60 mm
Plume expansion area custom size	--	11 mm
Nozzle area custom size	--	3 mm

3.1.3 Regions

The regions were set up to act like an open space so the plume could expand properly. All ambient boundaries were set to the free stream opposite flow supersonic conditions. The nozzle walls started as slip conditions for the first iterations but were later changed to no-slip conditions to obtain more realistic results (Figure 3.2) Initially,

the inlet ambient region was set as a stagnation pressure inlet (since it was going to withstand supersonic properties). However, this method kept resulting in floating point errors. This problem was solved by changing all ambient conditions to the same supersonic flow properties. Both methods are valid for this case, since the walls are far enough from the nozzle and don't affect the main plume expansion.
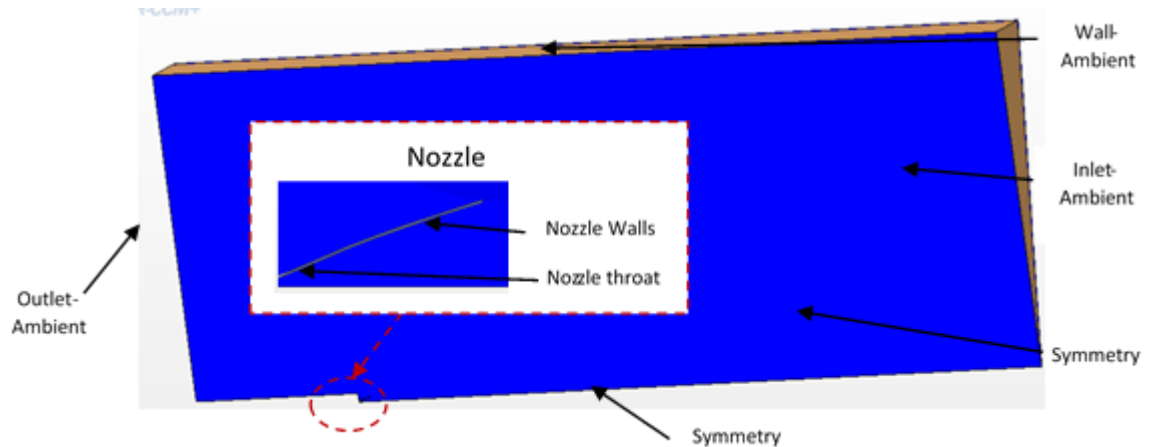
Figure 3.2- CFD model regions

3.1.4 Solvers

Star CCM used 4 different solvers for its calculations (Table 3.5). All of them come with predetermined setups, but can be changed depending on the problem. For this simulation, the coupled implicit option was changed during the iterations. In order to start the simulation, an Expert Initialization approach was used. Using this method helps the program solve the next iterations more easily. It starts the simulation with approximate numbers through the entire volume (including the appropriate plume expansion shape). The Courant number (CFL #) also varied through each case. The CFL # is a condition for stability to solve the partial differential equations and depends on the velocity, time step and length interval. It was higher for the first iterations to accelerate the convergence. But, it was decreased after about 3000 iterations to help the solver decrease the residuals. There were also some problems around the boundaries that could only be fixed by reducing the time step. Another option Star CCM offers is a Ramp approach for the Courant number. This is very useful since it starts decreasing after the solution starts converging but for this simulation case it wasn't a feasible option since it kept producing calculation errors.

Table 3.5- STAR CCM+ Solver options

Solvers
Partinioning
Wall Distance
Coupled Implicit
K- Omega turbulence

CHAPTER 4
RESULTS

4.1 Free stream results

The free stream case was the baseline of the analysis. This case assumed the plume expanded into a motionless flow with Mars ambient properties. The expansion could theoretically keep going if the exit boundary was even farther apart from the nozzle. However, this would create additional complications. As an example, the calculation time would increase and a more powerful computer would be needed to run a simulation with more cells. Nevertheless, the results obtained from this case (Figures 4.1, 4.2 and 4.3) are sufficient to be used as a comparison base for the following subsonic and supersonic cases. The Highest Mach number achieved is 9.7 about 1m away from the nozzle exit. The Mach number plot also shows the jet effect throughout the entire volume.
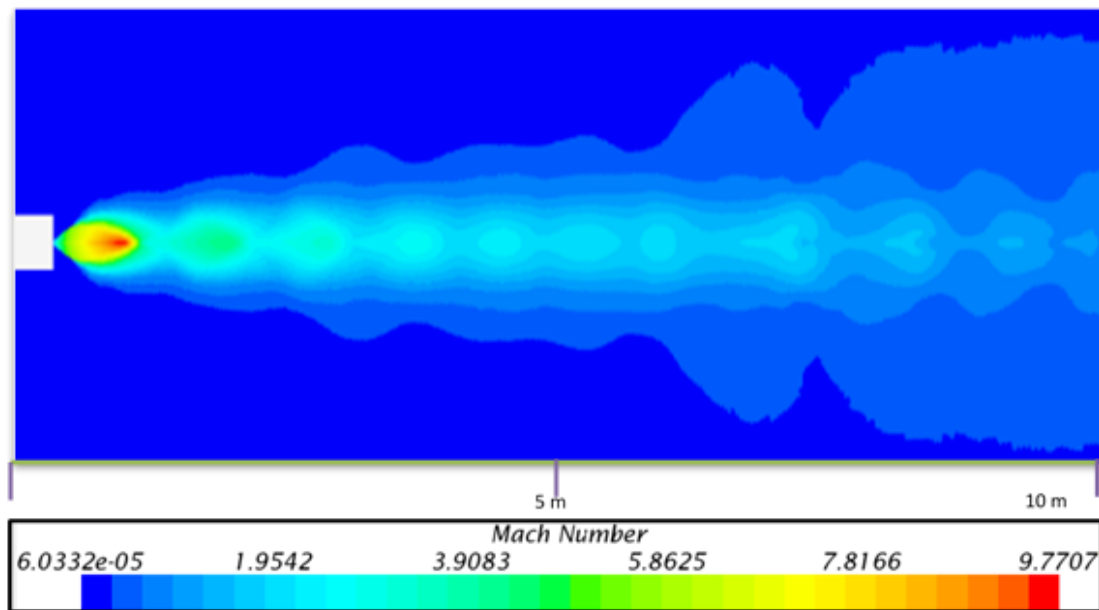
**Figure 4.1- Free Expansion Mach Number Plot**

The main jet plume expansion extends to about 1m from the nozzle exit plane. This value is taken as a point of comparison for the sonic and supersonic cases. The Pressure decreases from 88.1 to 0.04psi (ambient condition) over this distance. The pressure is slightly higher than the value input from the MMH properties (Table 2.6) due to the boundary layer around the nozzle walls. Also, the color bar states the lowest Pressure achieved is 0.016psi, which only occurs at few cells around the boundaries. The rest of the outside volume's Pressure is under the Martian atmospheric conditions input. This study attempts to prove that even at higher free stream Mach numbers, the main jet plume expansion (Figure 4.2) will not be significantly affected.
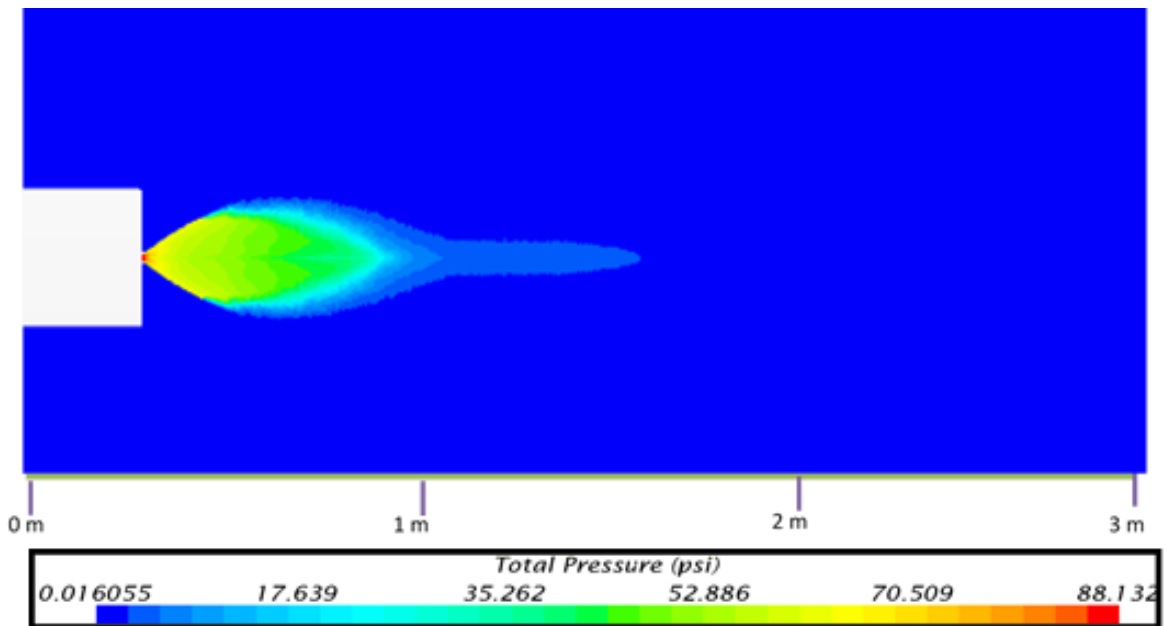
Figure 4.2- Freestream Total Pressure Plot

For freestream conditions, the temperature plot shows the flow still expanding past the boundary set up in the CFD model (Figure 4.3). Once the opposing flow is introduced, the temperature increases at the point of contact between the main jet plume and opposing flow. For supersonic opposing flow cases, the stagnation temperature reaches the nozzle throat max temperature.
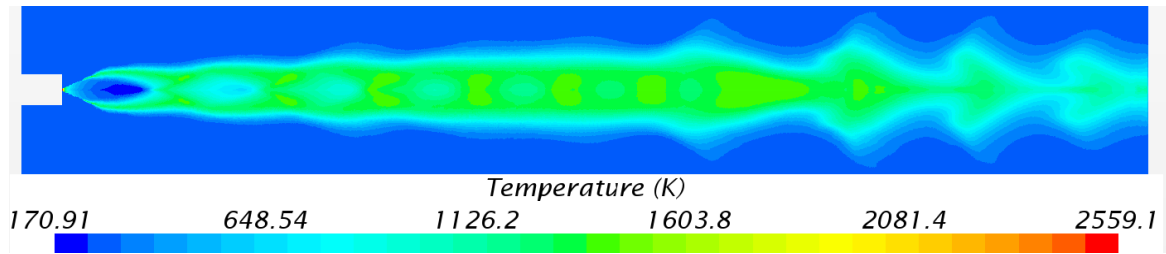
Figure 4.3- Freestream Temperature Plot

4.2 Comparison With Theoretical Results

The CFD free stream case was compared to the TDK results to ensure the values obtained were in an acceptable range. The two cases can't be exactly compared since they both represent different conditions (CFD software limitations). The CFD jet plume expands to Mars atmospheric conditions (Table 3.2), while the TDK analysis assumes it expands into vacuum conditions. Nevertheless, the results show that both analysis result in a similar Mach number, Static Pressure, and Temperature at the nozzle exit (Table 4.1). At Exit C, there is only a 10% difference in Mach number, but a 35% difference in Static Pressure and Temperature results. However, the main purpose of this comparison was to ensure the results were on the same order of magnitude for both cases rather than to directly compare the results.

Table 4.1- TDK and CFD results comparison

	Throat		EXIT A		EXIT B		EXIT C	
	TDK	CFD	TDK	CFD	TDK	CFD	TDK	CFD
$\dfrac{A_e}{A_t}$	1		15.033		50		100	
$Pstatic(psia)$	45	45.6	0.43	0.37	0.17	0.095	0.048	0.03
$T(Kelvin)$	3017	2600	3181	710	1183	510	360	240
$Mach\ number$	1	1	1.39	1.25	4.8091	5.1	5.5247	6.1

4.3 Mesh validation

The detailed mesh (Table 4.2) was validated by comparing the result obtained for the free stream case with an even finer mesh. This new finer mesh took more than twice the time to run compared to the base mesh. Additionally, the computer power required to perform these calculations was very close to exceeding in-house capabilities. The results were very similar between both cases, but the finer mesh can certainly be described as more accurate. Unfortunately, the increase in calculation time overshadows this improvement.

Table 4.2- Mesh validation set up

|	Mesh base	Finer Mesh
Total number of cells	2388370	5123420
Base size	60 mm	40 mm
Plume expansion area custom size	11 mm	8 mm
Nozzle area custom size	3 mm	2 mm
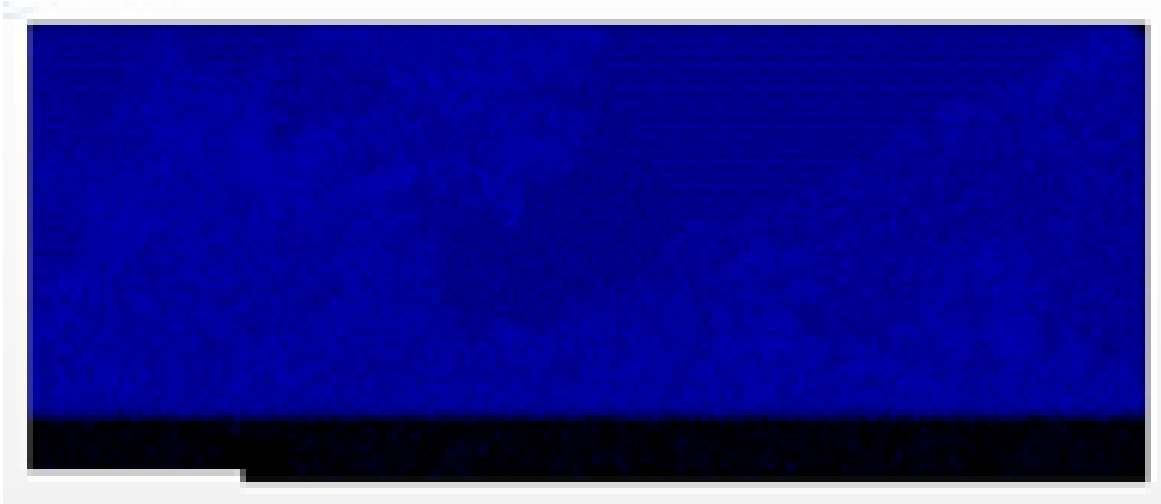
Figure 4.4 - Finer mesh

Table 14 provides a quantitive comparison of the results obtained for both mesh cases. The Highest Total Pressure doesn't change between models (Table 4.3), even though the Pressure plot shows a more elongated shape (Figure 4.5). This shape indications the jet plume expansion reaches approximately half a meter more than what the previous mesh shows. However, the Pressure is already low enough at this distance to

not cause any significant changes in the overall results. The Highest Mach number and Total Temperature show a small difference (Table 4.3). This difference was expected, but it's small enough to demonstrate the capabilities of the base mesh selected.

Table 4.3- Mesh validation results

|	Mesh base	Finer Mesh	% Difference
Highest Mach number	9.77	10.016	2.5
Highest Total Pressure (psi)	88.132	88.132	0
Highest Total Temperature (K)	2559.1	2924.9	13
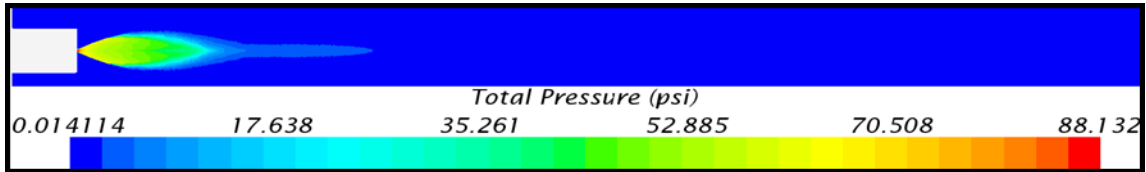
**Figure 4.5- Finer Mesh Total Pressure Plot**

4.4 Subsonic and Sonic Cases

4.4.1 Mach 0.5 Case

The subsonic cases were analyzed after the free stream case converged properly. Increments of 0.1 Mach every 3000 iterations were used to go from free stream conditions to Mach 0.5 due to the solver initially having difficulties properly converging directly to Mach 0.5. This method increased the calculation time, but it provided more accurate result. The total pressure plot (Figure 4.6) shows that the main plume expansion doesn't change compared to the free stream conditions, since the main jet plume still expands 1.5 m away from the nozzle.
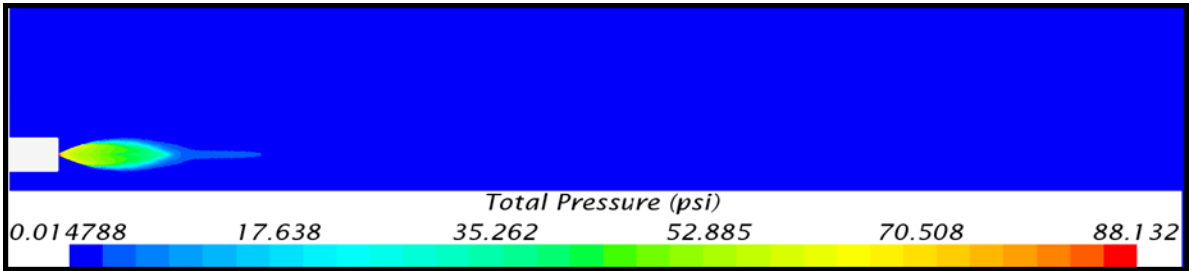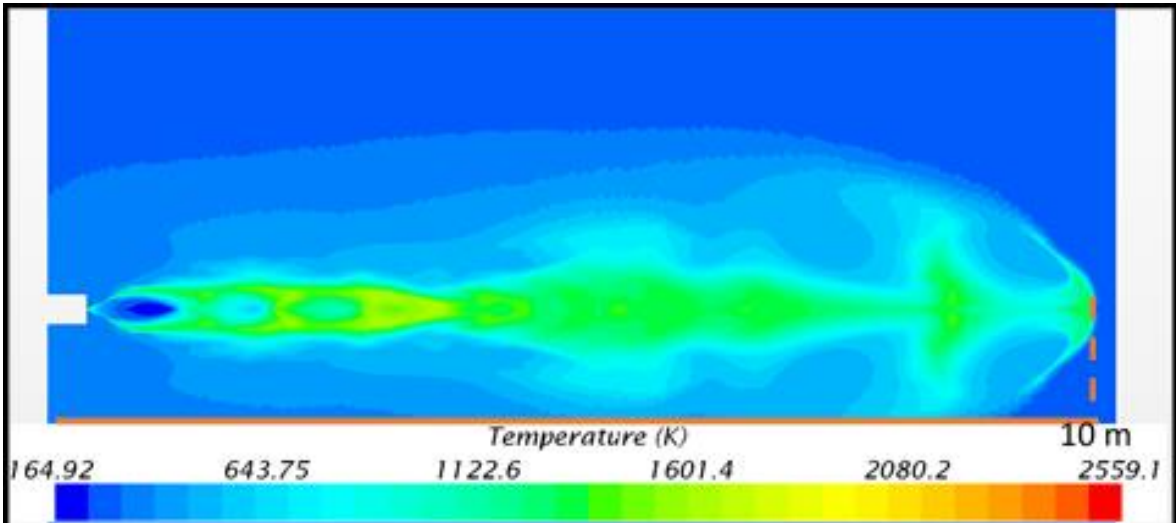
Figure 4.6- Mach 0.5 Pressure Plot

The Mach plot also starts changing at subsonic speeds, and since the jet flow can't keep expanding, a shock appears where the jet flow and opposing flow interact (Figure 4.7). It is not as clear in this graph because of the exit boundary distance. However, it is more clearly seen in the following sonic and supersonic cases. This shock will also be displaced closer to the motor nozzle as the opposite flow Mach number increases.
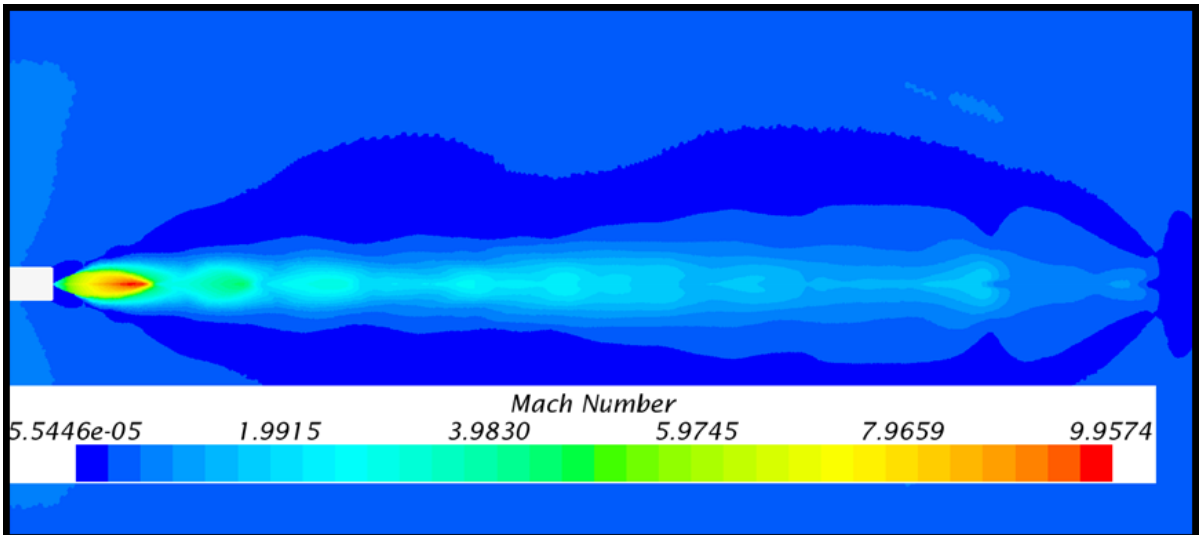

Figure 4.7- Mach 0.5- Mach Plot

The Temperature plot (Figure 4.8) provides a clearer representation of the shock created by the jet flow and opposing flow. At Mach 0.5, this shock is still 10m away from the nozzle, therefore it would not cause any problems to any components in the same plane as the nozzle. The highest temperature achieved is 2559 K which still happens at the nozzle throat, however, an increase in temperature is already shown at the shock. This is not as high as the throat temperature because of dissipation in low Mach number cases.

Figure 4.8- Mach 0.5 Temperature plot

4.4.2 Mach 1.0 Case

At Mach 1, the Pressure plot still shows no effect of the opposing flow in the main jet plume expansion (Figure 4.9). The jet flow still expands the same distance as for the subsonic and free stream case. However, the lowest Pressure achieved is 0.005 psi higher than in the free stream case. This difference is almost negligible compared to the high Pressure at the nozzle throat (88 psi).
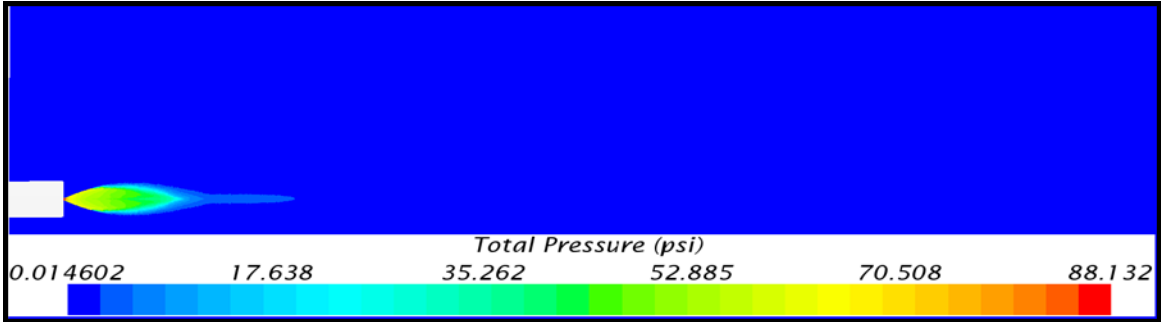
**Figure 4.9- Mach 1.0 Pressure Plot**

The Mach Plot provides a more defined shape for the shock created by the opposing flow. It is also slightly closer to the nozzle exit, but still far enough away to not cause any damage to components on the same plane. The Highest Mach number achieved occurs at the same distance as for previous cases, but is 0.02 higher. There are many

possible reasons for this, but the most probable one is the more acute convergence caused by the increased number of iterations.
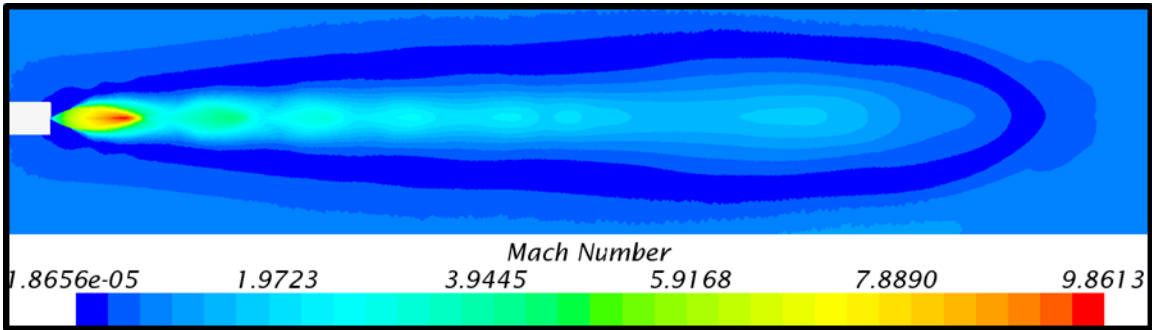
Figure 4.10- Mach 1.0- Mach Plot

The temperature plot (Figure 4.11) still shows some dissipation, but the shock location is much clearer than in previous cases. At this point, the temperature is around 2000 K, which is closer to the 2559K that would result from a case with no heat dissipation.
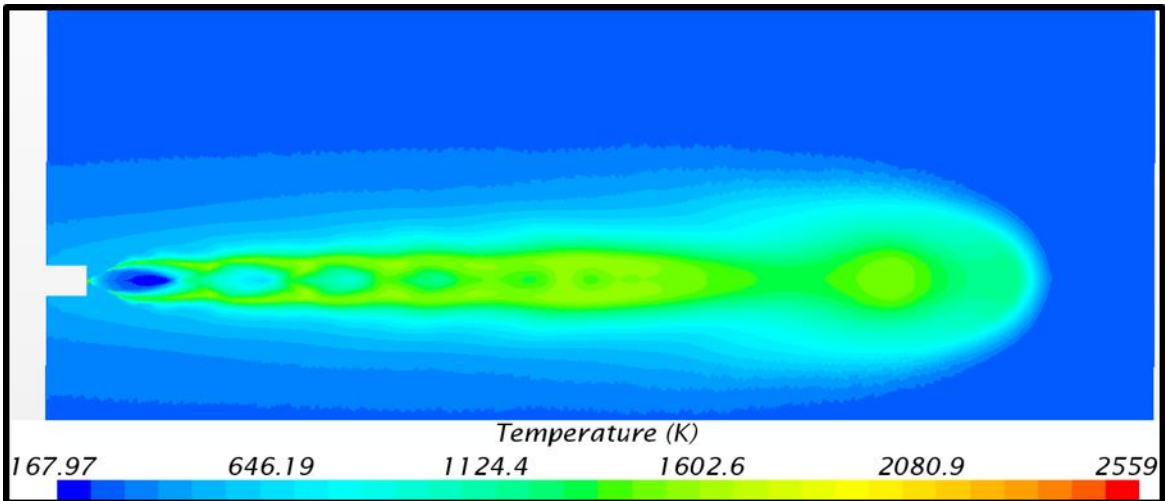
Figure 4.11- Mach 1.0 Temperature Plot

For now, propulsion is only used once subsonic speeds are achieved. However, the sonic case results from this CFD analysis are evidence that for upcoming missions, the propulsion system could be improved for higher performance. The effects the opposing flow have on the main jet flow are negligible since the main shock is about 9m away from the nozzle plane. The spacecraft would likely not be affected at this distance, making sonic retro propulsion a feasible option for future Mars landings.

CHAPTER 5

Supersonic Cases Results

5.1 Supersonic Cases Overview

The Opposing flow supersonic cases reflected below are the product of numerous iterations and methods of calculations. Once the opposing flow Mach number exceeded 1.0, the solver started having problems with the iterations steps. This was solved by decreasing the starting CFL # to 3. Keeping this low CFL # would have increased the calculation time significantly, so it was increased back to 5 after about 5000 iterations. This was a slow calculation, but in the end provided the results expected. Another method applied to the simulation was changing the outside boundary conditions. Occasionally it is easier for the solver to begin with stagnation inlets for Supersonic flow. Even though this method was previously tried and rejected for subsonic conditions, it proved to be the most ideal for supersonic conditions. After the solution was converged, the outside boundaries were changed back to free stream to ensure both would provide the same results.
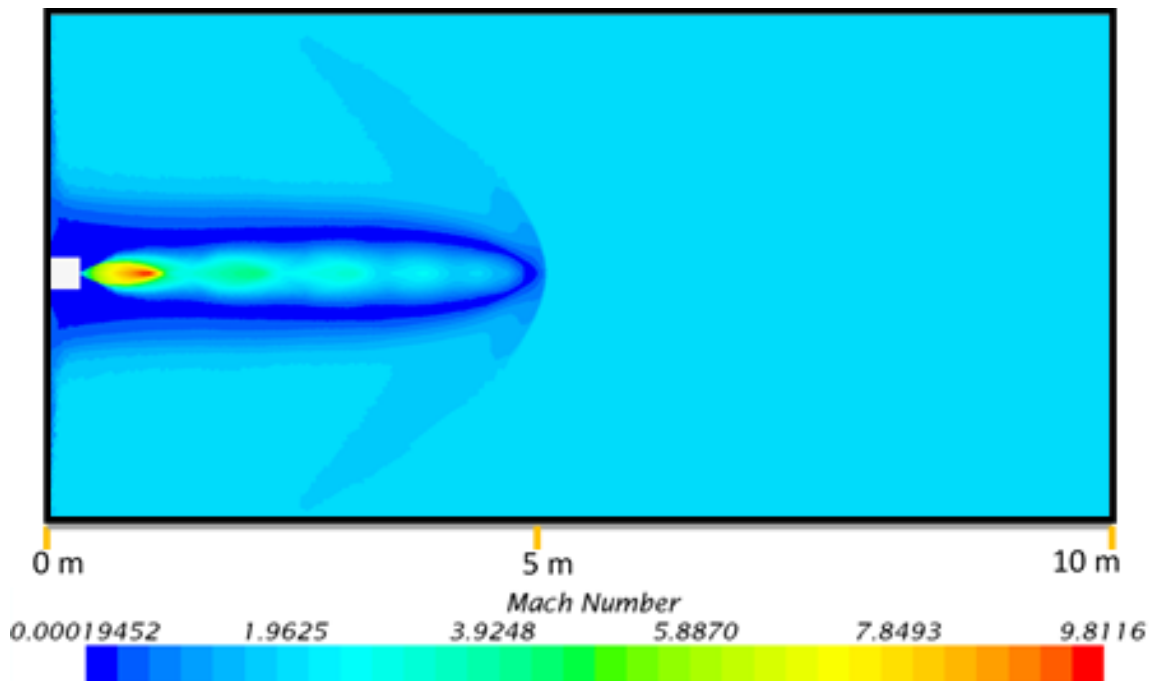
5.2 Mach 2.0

At Mach 2.0, the Pressure Plot shows no effect on the main jet plume expansion. The Pressure range still varies from close to ambient to the highest at the nozzle throat. The lower values increased slightly compared to the sonic case. However, this difference is still less than 0.02% from the Throat Total Pressure (Figure 5.1).
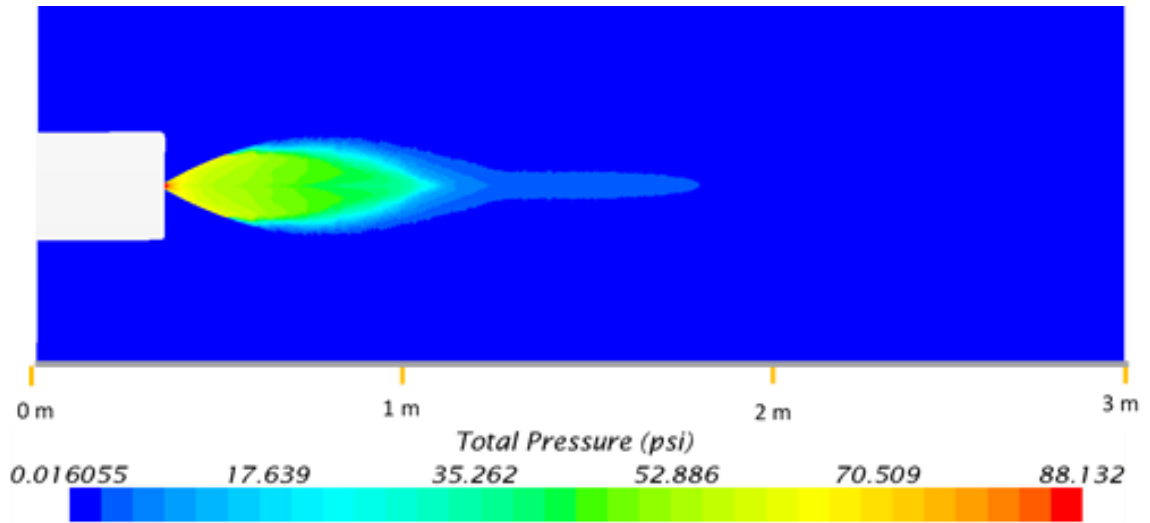
Figure 5.1- Mach 2.0 Total Pressure

For this supersonic case, the plume still extends 5m from the nozzle. At this point, the shock between the opposing flows can be seen clearly in the Mach Plot (Figure 5.2). However, this is still far enough to not create any problems to the spacecraft located on the nozzle plane.


Figure 5.2-Mach 2.0- Mach Plot

Since there is less time for heat dissipation for higher free stream Mach numbers, the stagnation temperature at the shock equals the maximum total temperature at the nozzle throat (Figure 5.3). This is not a problem because of the distance away from the place this occurs at.

Figure 5.3-Mach 2.0 Temperature Plot
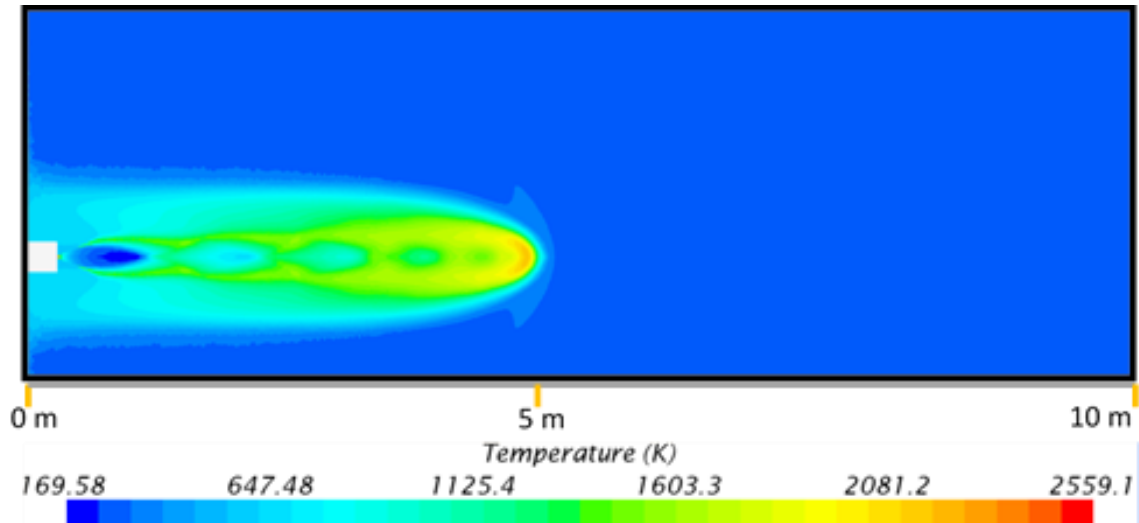
The Velocity Streamlines graph (Figure 5.4) is a good overall representation of the opposite flow Mach 2.0 case. Outside the plume expansion volume, the streamlines all have the same direction and values. This demonstrates that the outside "box" volume created originally is sufficient for this analysis. Another proof of the model's reliability is the plume expansion's overall shape.


Figure 5.4- Mach 2.0 Velocity Plot
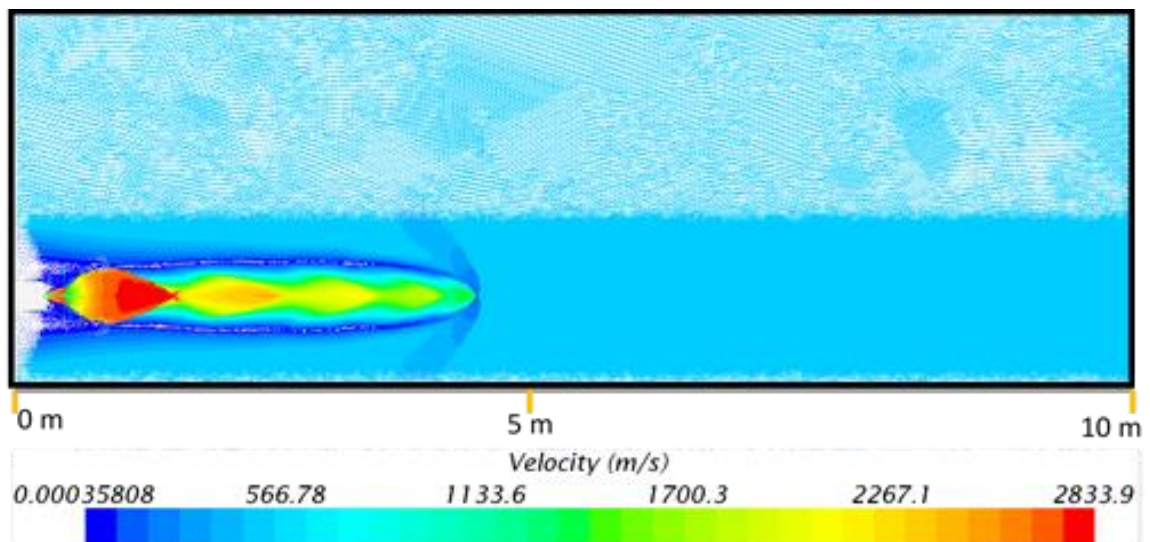
5.3 Mach 3.0

       Mach 3.0 was the highest value analyzed for this study. This number wasn't chosen arbitrarily, since this is the point at which the parachute was ejected during the MSL Mars mission. The pressure plot (Figure 5.4) shows the main jet plume expansion to be exactly as it was in previous cases. This proves that SRP could be used for future Mars landings without any effect on the main jet flow expansion.
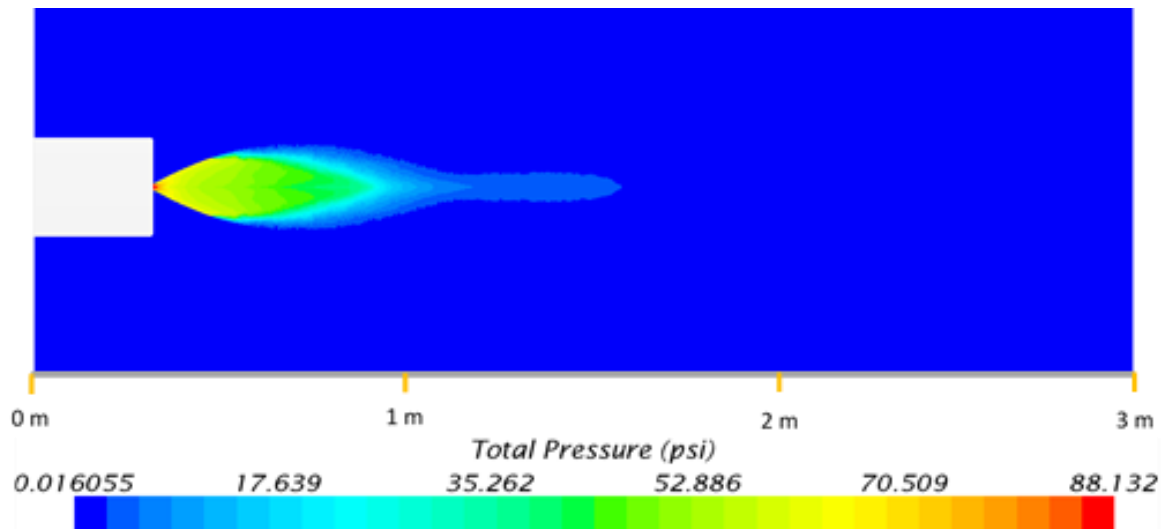

Figure 5.5- Mach 3.0 Pressure plot

       The Mach plot (Figure 5.5) demonstrates that even at this high Mach number, the plume extends 2m away from the nozzle plane. The plume expansion decreased through all the cases as the opposite free stream flow Mach number increases. However, the distance is still large enough to not cause any direct interference with the spacecraft.
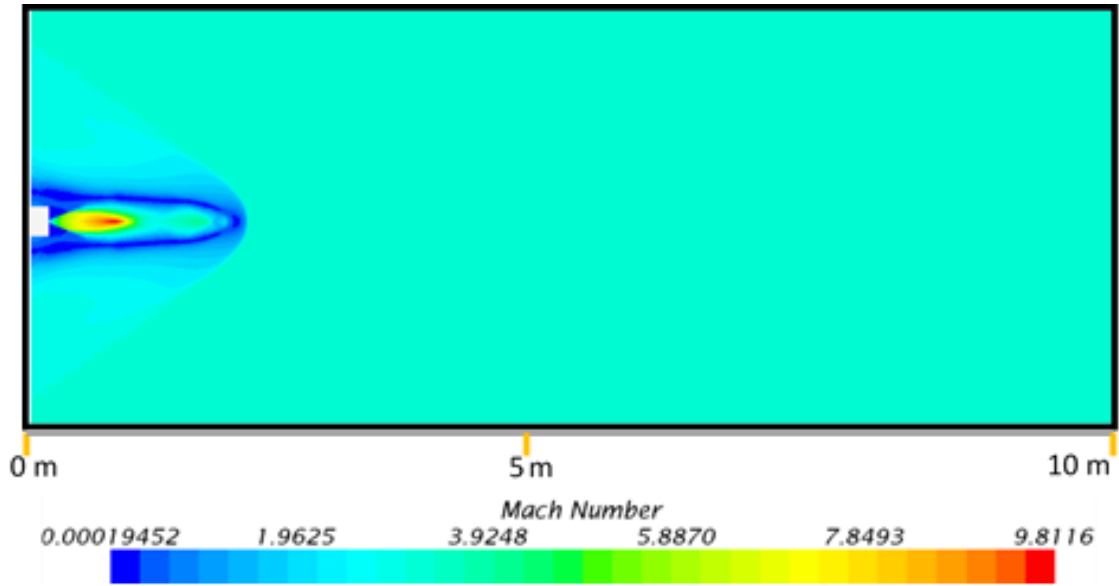
Figure 5.6- Mach 3.0 Mach Plot

At the point of the shock between the opposing flows, the Temperature is clearly as high as the nozzle throat (Figure 5.6). This high temperature could have some impact on the spacecraft heat shield. However, this should be negligible due to the distance from the spacecraft and materials used.
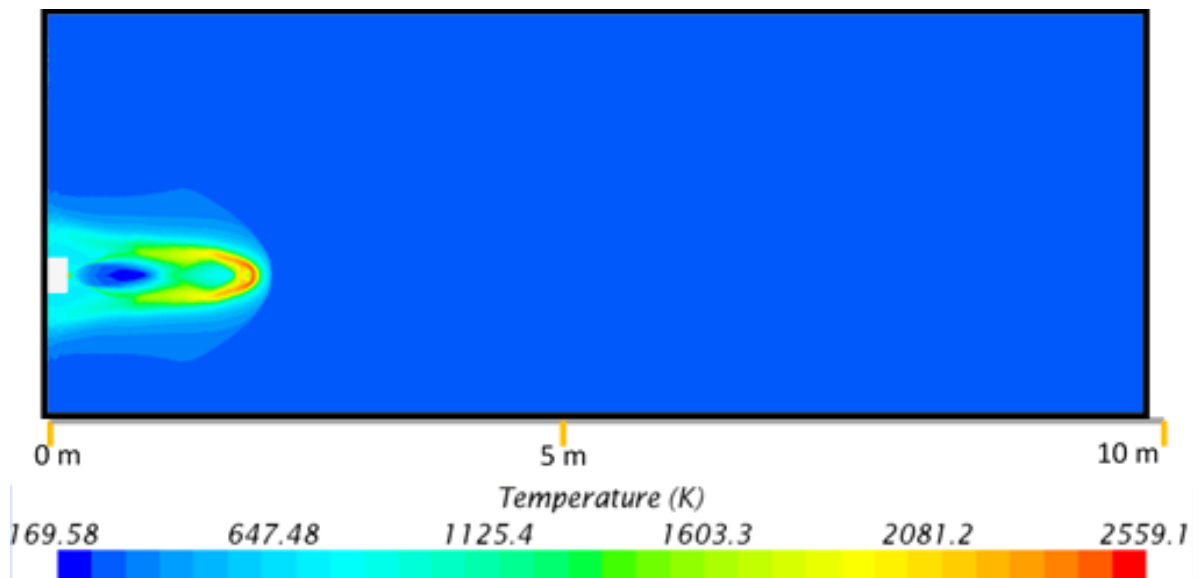
**Figure 5.7- Mach 3.0 Temperature Plot**

The Velocity Plot (Figure 5.6) is also used to demonstrate the analysis reliability. It is similar to the Mach 2.0 (Figure 5.4), except for the distance the jet plume expands. This distance was reduced to half by increasing the opposing flow Mach number by 1. This has the potential to create problems at very high Mach numbers, but not for those covered in the scope of this research.
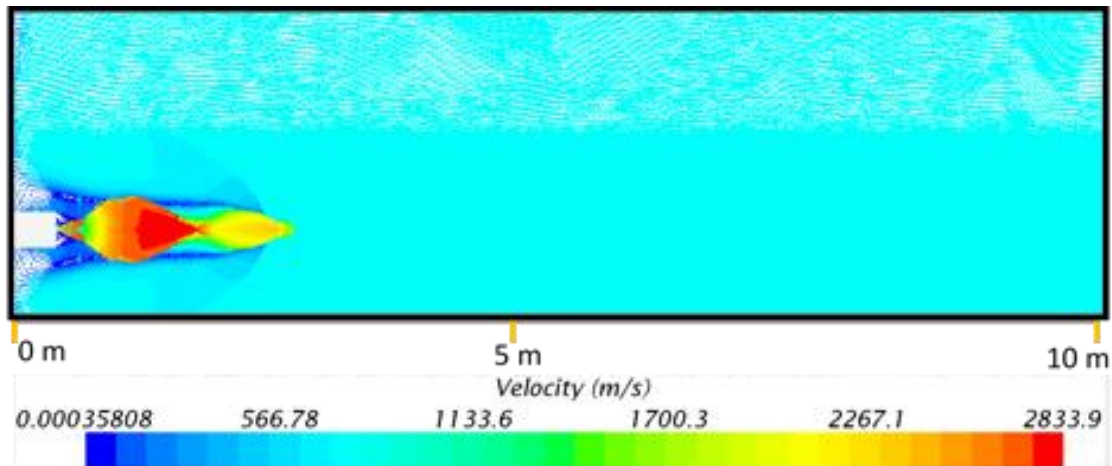
Figure 5.8- Mach 3.0 Velocity Plot

5.4 Results Analysis

The results obtained from each opposite flow Mach number case demonstrate the feasibility of including SRP in the next Mars landing. The primary jet flow expansion is not affected even at the higher Mach number case studied. The Pressure only begins to change at 2m away from the nozzle plane, when it is only around 3% of the Nozzle throat Pressure (Figure 5.8). This shows that even at Mach 3, the pressure created by the opposite flow is not significant compared to the main jet flow pressure. Additionally, higher Mach numbers will follow similar patterns to those presented by the Mach 3 case. The Maximum temperature is still about 2m away from the motor plane. At this distance, the temperature is still not a big concern based on the materials used for previous missions.
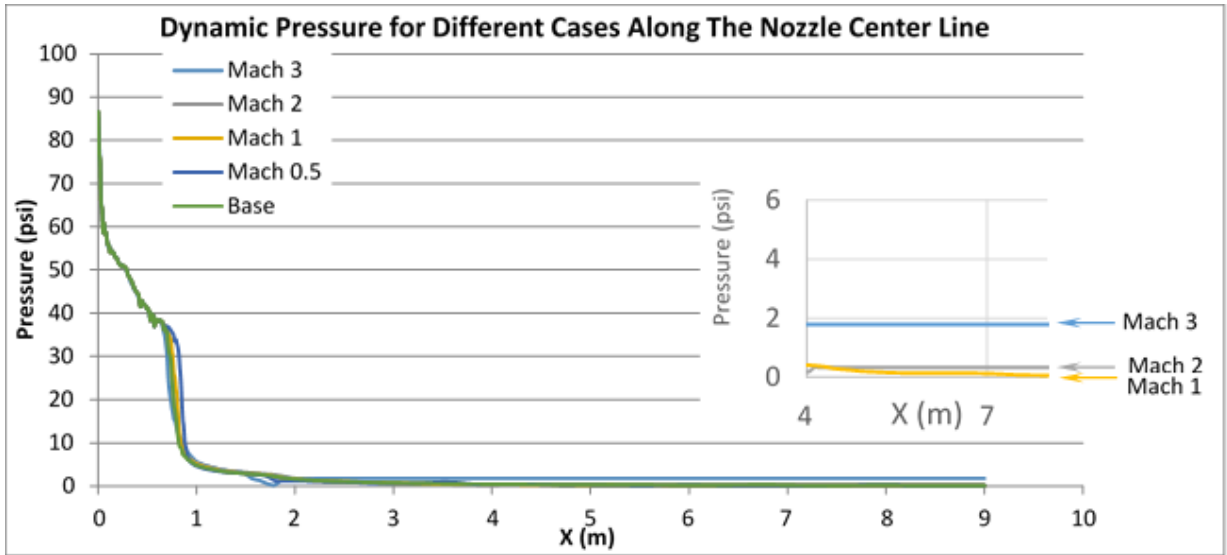
Figure 5.9- SRP Final Pressure Plot

CHAPTER 6
CONCLUSIONS

The CFD work presented in this research illustrates the feasibility of using Supersonic Retro-Propulsion technology in upcoming Mars missions. The conditions in the red planet's atmosphere were simulated as closely as possible using the chosen CFD tool. However, CFD analysis alone cannot provide proof that SRP will work under these environment, and further testing is required to obtain certainty. Recent tests by Space Exploration Technologies (SpaceX) prove that SRP is no longer just a concept viable for Earth conditions, but Mars SRP is yet to be demonstrated ("*Elon Musk on SpaceX's Reusable Rocket Plans*").

NASA is investing more time and resources in new EDL techniques that will assist human exploration. Unfortunately, using a parachute and subsonic retro propulsion has limited applications (Figure 6.1). The mass limit it imposes has already been met, but SRP is a viable method to increase it. Before this technology is ready for development, more tests need to be performed in order to validate the CFD results. A number of these experiments have already been or are being performed at various NASA research centers, including sub-scale wind tunnel tests that will help compare tests and CFD data to full scale engine and vehicle performance tests. The goal is to demonstrate SRP in Mars atmosphere within the next 10 years, which seems immediate compared to the volume of work needed to have it ready. For starters, more ground testing, engine performance tests and CFD models for the different set ups should be explored. Once these basic cases have been analyzed, the entire vehicle configuration needs to be studied to find the optimum number and location for the engines.
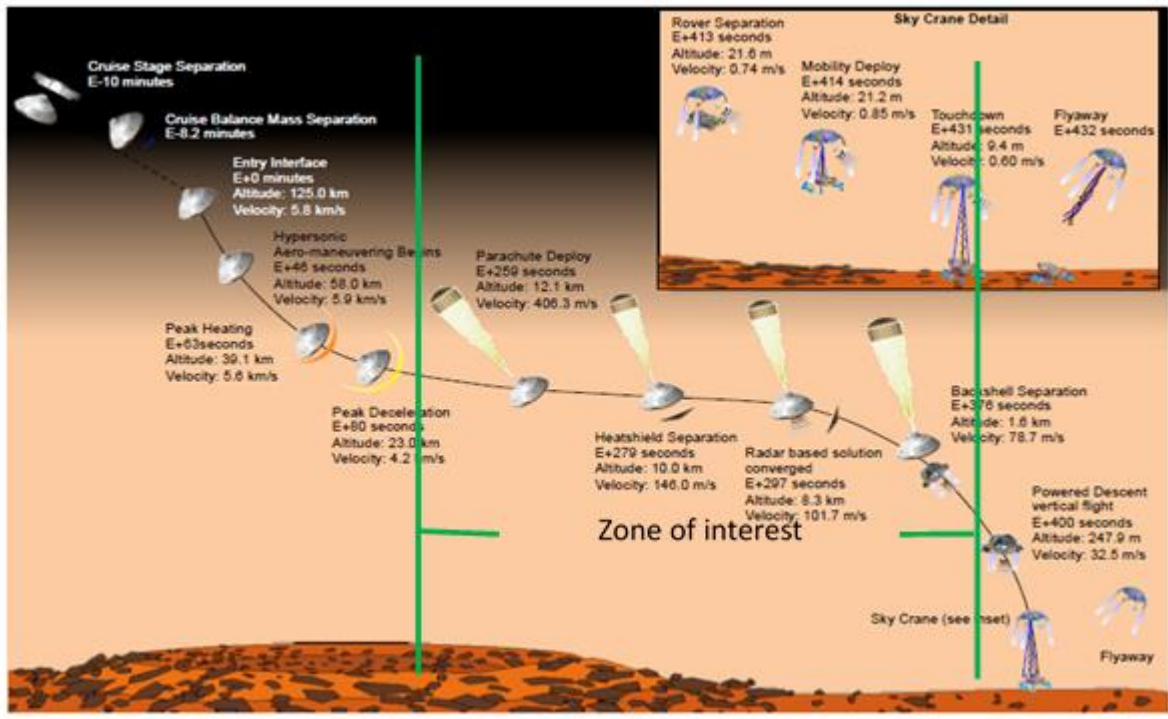
Figure 6.1- Current EDL technology

CHAPTER 7
Recommendations for Future Work

This project only takes into account a single nozzle configuration. However, a full analysis with multiple nozzles is required if SRP is to be viable for future missions. The jet plumes will not only interact with the opposing ambient flow, but with each other depending on the engine locations. This could create design challenges in the future and will require more testing and analysis.

More details can also be added to this model to ensure accuracy. One way of achieving this would be adding the remaining mixture, however this will increase the computational time and power needed exponentially, while only increasing the accuracy slightly. A more imperative improvement would be to run a transient analysis in addition to the steady state analysis presented here. This new simulation would model the engine start up under SRP conditions, which is one of the most pertinent questions that needs addressing. Engine start-up has already been proven under Earth conditions, but it is unclear as to whether Mars atmosphere will allow the same.

The final improvement recommended would be increasing the opposite flow Mach number. This project focused on comparing SRP to the current EDL preferred technique. The parachute on MSL was deployed at a Mach number of approximately 2, which was easily achieved using the SRP single nozzle design presented. However, the requirements for the next Mars missions will not be the same and may call for the use of an additional EDL method before slowing down to Mach 2.

Bibliography

[1]. Bakhtian, N. M., and Aftosmis, M. J., "*Parametric Study of Peripheral Nozzle Configurations for Supersonic Retropropulsion*," Journal of Spacecraft and Rockets, Vol. 47, No.6, 2010.

[2]. Braun, R.D., and Manning, R.M., "*Mars Exploration, Entry, Descent and Landing Challenges*," Journal of Spacecraft and Rockets, Vol. 44, No. 2, 2007.

[3]. Charczenko, N., and Hennesey, K. W. "*Investigation of a Retrorocket Exhausting from the Nose of a Blunt Body into a Supersonic Freestream*," NASA TN D-751, September 1961.

[4]. Cordell, C. E. *Computations Fluid Dynamics and Analytical Modeling of Supersonic Retropropulsion Flowfield Structures Across a Wide Range of Potential Vehicle Configurations*, Diss, Georgia Institute of Technology, 2013.

[5]. Edquist, K. T., et al., "*Development of Supersonic Retro-Propulsion for Future Mars Entry, Descent and Landing Systems*," AIAA Paper 2010-5046, July 2010.

[6]. Gnoffo, P. A., "*Planetary-Entry Gas Dynamics*," Annual Review of Fluid Mechanics, Vol. 31, 1999.

[7]. Jarvinen, P.O., and Adams, R. H., "*The Aerodynamic Characteristics of Large Angled Cones with Retrorockets*," NASA 7-576, February 1970.

[8]. Korzun, A. M., Braun, R. D., and Cruz, J. R., "*Survey of Supersonic Retropropulsion Technology for Mars Entry, Descent and Landing*," Journal of Spacecraft and Rockets, Vol. 46, No5, 2009.

[9]. Orth, R. C., Schetz, J. A., and Billig, F. S., "*The Interaction and Penetration of Gaseous Jets in Supersonic Flow*," NASA CR-1386, July 1969.

[10]. Sutton, G. P., and Biblarz, O., *Rocket Propulsion Elements*, 8th ed, Hoboken: Wiley, 2010. Print.

[11]. Zang, T. A., "*Entry, Descent and Landing Systems Analysis Study: Phase 1 Report*," EDL Systems Analysis Team, NASA, July 2010.

[12]. "*Elon Musk on SpaceX's Reusable Rocket Plans*," Popular Mechanics, February 2012.

[13]. "STARCCM+ Manual," August 2014. steve.cd-adapco.com [retrieved August 2014]